Downloaded from orbit.dtu.dk on: May 06, 2023

DTU Library

Ultra-Efficient and Broadband Nonlinear AlGaAs-on-Insulator Chip for Low-Power Optical Signal Processing

Pu, Minhao; Hu, Hao; Ottaviano, Luisa; Semenova, Elizaveta; Vukovic, Dragana; Oxenløwe, Leif Katsuo; Yvind, Kresten

Published in:
Laser & Photonics Reviews

Link to article, DOI:
10.1002/lpor.201800111

Publication date:
2018

Document Version
Peer reviewed version

Link back to DTU Orbit

Citation (APA):
Pu, M., Hu, H., Ottaviano, L., Semenova, E., Vukovic, D., Oxenløwe, L. K., & Yvind, K. (2018). Ultra-Efficient and Broadband Nonlinear AlGaAs-on-Insulator Chip for Low-Power Optical Signal Processing. *Laser & Photonics Reviews*, *12*(12), [1800111]. https://doi.org/10.1002/lpor.201800111

General rights
Copyright and moral rights for the publications made accessible in the public portal are retained by the authors and/or other copyright owners and it is a condition of accessing publications that users recognise and abide by the legal requirements associated with these rights.

- Users may download and print one copy of any publication from the public portal for the purpose of private study or research.
- You may not further distribute the material or use it for any profit-making activity or commercial gain
- You may freely distribute the URL identifying the publication in the public portal

If you believe that this document breaches copyright please contact us providing details, and we will remove access to the work immediately and investigate your claim.

Original Paper

Ultra-efficient and broadband nonlinear AlGaAs-on-insulator chip for low-power optical signal processing

Minhao Pu, Hao Hu, Luisa Ottaviano, Elizaveta Semenova, Dragana Vukovic, Leif Katsuo Oxenløwe, and Kresten Yvind**

*Corresponding Authors: E-mail: mipu@fotonik.dtu.dk, kryv@fotonik.dtu.dk

DTU Fotonik, Department of Photonics Engineering, Technical University of Denmark, Ørsteds Plads 343, DK-2800 Lyngby, Denmark

Abstract: Four-wave mixing is a versatile optical nonlinear parametric process that enables a plethora of signal processing functionalities in optical communication. Realization of efficient and broadband all-optical signal processing with ultra-low energy consumption has been elusive for decades. Although tremendous efforts have been put into developing various material platforms, it has remained a challenge to obtain both high efficiency and broadband operation. In this paper, we present an aluminum gallium arsenide nonlinear chip with the highest four-wave mixing conversion efficiency per length per pump power and an ultra-broad bandwidth. Combining an ultra-high material nonlinearity and the strongest effective nonlinear enhancement from a high-index-contrast waveguide layout, an ultra-high conversion efficiency of -4 dB is obtained in a 3-mm-long nano-waveguide. Taking advantage of high-order dispersion, a new scheme is presented to realize an ultra-broad continuous conversion bandwidth covering 1280-2020 nm. A microresonator is also utilized to demonstrate a conversion efficiency enhancement gain of more than 50 dB with respect to a waveguide device, which significantly reduces the power consumption. Moreover, wavelength conversion of an optical serial data signal is performed at a bit rate beyond terabit-per-second, showing the capabilities of this III-V semiconductor material for broadband optical signal processing.

1. Introduction

Supported by the millions of kilometers of optical fiber spun around the world, the internet traffic is incessantly growing, and all connections are constantly requiring higher bandwidth. All active signal processing of the transmitted optical data is performed electronically today after optical-to-electrical conversion of parallel channels, each at data rates within the bandwidth allowed by electronics, typically up to around 100 GHz. With continuous traffic growth, the amount of active signal processing follows suit, and there may be a need for fewer but more efficient parallel signal processors. Such processors may be optical signal processors, as such can operate at speeds far above that of electronics[1] and cover bandwidths in excess of the used telecom wavelength bands, thus enabling massively parallel signal processing in a single device. For these reasons, optical signal processing (OSP) is subject to extensive ongoing research involving the exploration of various nonlinear optical effects and various nonlinear optical materials harnessed and demonstrated for several specific simple signal processing functionalities. A commonly used nonlinear optical effect is four-wave mixing (FWM), owing to its transparency to data format and the preservation of coherence. FWM is based on the generation of Stokes and anti-Stokes photons from two pump photons obeying the energy and momentum conservation through the third-order susceptibility. The nearly instantaneous response (femtosecond scale) of the parametric process potentially enable processing data signals at speed beyond terabit-per-second (terabaud symbol rates). Applying different pumping schemes, one can use the FWM process for various applications, such as wavelength conversion, parametric amplification, signal regeneration, waveform sampling, switching, de-multiplexing, and optical phase conjugation.

High-performance FWM demonstrations have been made in highly nonlinear fibers (HNLFs)[2] normally with tens of meters length due to a relatively low material nonlinearity. Following the trend of device miniaturization, nonlinear OSP has also been extended from HNLF to integrated

platforms[3] where the combination of a high intrinsic nonlinearity and strong light confinement leads to an ultra-high effective nonlinearity. Figure 1a shows the schematic illustration of an example of an OSP application, namely all-optical wavelength conversion using a degenerate FWM process in a nonlinear photonic chip. With the presence of a strong continuous-wave optical pump beam (green) in a nonlinear waveguide, the binary data encoded on the intensity signal pulses (blue) can be replicated to idler pulses (red). Two pump photons and one signal photon interact to create an idler photon, and by energy conservation, the idler photon will be at a new optical frequency. Since the idler pulse intensity is proportional to the product of the intensities of the interacting waves and the phase is a linear combination of those of the interacting waves, such a conversion offers strict transparency with respect to modulation formats by preserving phase and amplitude information.

An ideal integrated nonlinear platform would display both a high conversion efficiency and a continuous broad conversion bandwidth. Though early efforts made on the silicon-on-insulator (SOI) platform showed promising results,[4–7] the SOI devices suffer from the two-photon-absorption (TPA) induced free-carrier absorption (FCA) at the telecommunication wavelengths. Since the FWM and TPA scale the same way with power, the presence of TPA severely limits the application of this and other platforms suffering from TPA. To quantify the performance of different material platforms for OSP applications at low-power operation conditions, we use a figure of merit (FOM), defined by the ratio of the nonlinear coefficient (or effective nonlinearity) to attenuation coefficient.[8] Note that the FOM used in this paper is different from the TPA-related FOM, which is defined to be proportional to the ratio of material nonlinearity and TPA coefficient, and is commonly used for materials with small bandgaps.[3] The TPA-related FOM reflects material properties (and is infinite in all TPA free materials) while the FOM used in this paper emphasizes the overall efficiency of a waveguide platform. Targeting a higher FOM, a variety of integrated material platforms[9–23] have been proposed and developed. However, it is rather challenging to enhance the FOM as improving

one of the parameters is often associated with a degradation of the other. The waveguide linear and nonlinear loss can be reduced by using low index materials with very large bandgaps, [9–14] where the mature fabrication and the low-index contrast waveguide layout ensure a small scattering induced by the sidewall roughness. However, the overall FWM performances are then limited by a reduced effective nonlinearity, which is defined by $\gamma=\omega n_2/cA_{eff}$, where n_2 is the material's intrinsic nonlinear index, A_{eff} is the area of the propagating mode, c is the speed of light and ω is its angular frequency. On the other hand, the device effective nonlinearity can be increased by either engineering the material[17–23] to enhance the intrinsic nonlinearity or by structural engineering of the nonlinear medium to enhance the light-matter interaction using resonant effects like in photonic crystal waveguides (PhCW)[24] or microresonators.[25–31] The challenges for the material engineering approach, lies in the fabrication concerning high-quality material synthesis and device patterning. In addition, the structural engineering approach yields a limited operation bandwidth for PhCWs (operation linewidth for microresonators). For non-resonant straight waveguides, the FWM conversion bandwidth can be increased by careful dispersion engineering.[5,6] It is, however, challenging to simultaneously push both conversion efficiency and bandwidth since they are correlated via the nonlinear interaction length. In spite of tremendous efforts made in developing new material platforms in the last decade, the achievable maximal efficiency-bandwidth product has not been significantly improved yet.

In this paper, we achieve a significant improvement of the conversion efficiency-bandwidth product. We present a recently developed integrated material platform, which offers low linear and nonlinear material absorption, large intrinsic nonlinearity, strong light confinement, and mature patterning technologies. We present a universal scheme for highly nonlinear waveguide platforms to generate an ultra-broad continuous conversion band. Benefitting from the improved FWM performance, we experimentally realize all-optical wavelength conversion of optical serial data

signals at a data speed beyond THz pulse rates (terabaud symbol rates). A tremendous power consumption reduction is also demonstrated in a GHz-linewidth microresonator, showing potential for realizing ultra-low power, monolithically integrated optical signal processors.

2 Materials and Methods

Aluminum gallium arsenide ($Al_{1-x}Ga_xAs$) is a semiconductor material, which has been widely used in double heterostructure devices like GaAs/AlGaAs lasers. Leveraging the mature growth technology developed for semiconductor lasers, high-quality AlGaAs thin films can be epitaxially grown on lattice-matched substrate materials such as GaAs. AlGaAs exhibits a high intrinsic Kerr (third-order) nonlinearity (on the order of 10^{-17} m^2W^{-1}, higher than silicon) and has been proposed for nonlinear processes since 1994.[32] Moreover, the material bandgap of $Al_{1-x}Ga_xAs$ can be engineered by changing the aluminum concentration (x) in such a way that the bandgap is sufficiently large to avoid TPA in the 1550nm range while the material nonlinearity is maintained at a high level.[33] Although the high linear index (similar to silicon) makes AlGaAs potentially suitable for high-confinement nano-waveguides, the conventional deep-etched AlGaAs waveguides exhibit low effective nonlinearity due to the vertical low-index contrast waveguide layout. To take full advantage of the high intrinsic linear and nonlinear index of the AlGaAs material, we transferred the conventional AlGaAs waveguide layout into a high index contrast layout, by realizing the AlGaAs-on-insulator (AlGaAsOI) platform.[34] Note that a quadratic (second-order) nonlinearity also exists in AlGaAs due to a non-centrosymmetric crystal structure. However, the phase-matching requirement for the quadratic nonlinear processes [35] is quite different from that for the Kerr processes, so we can focus on the Kerr nonlinearity in this paper.

The AlGaAsOI wafer, where a high-quality thin AlGaAs film on top of a low-index insulator layer (SiO_2) resides on a semiconductor substrate, is fabricated through wafer bonding and substrate removal processes.[36] The AlGaAsOI nano-waveguides are defined using an optimized electron-

beam lithography process and a boron trichloride (BCl_3)-based dry etching process. Figure 1b shows the scanning electron microscopy (SEM) picture of a fabricated AlGaAsOI nano-waveguide before it is clad by insulating materials such as SiO_2 or Al_2O_3 (see Supporting Information). A smooth sidewall patterning and a high-quality crystal growth ensure low scattering and low material absorption, resulting in a low linear loss device. Thanks to the large index difference (~1.8) between AlGaAs and glass, the light can be strongly confined within the sub-micron core as shown in Figure 1b, which not only enhances its device effective nonlinearity but also enables an efficient dispersion engineering. With such strong light confinement, ultra-efficient nonlinear devices can be made with a small footprint. Figure 1c shows such an AlGaAsOI photonic chip accommodating hundreds of nonlinear waveguides, yet only covering less than half the area of a one euro coin.

3 Results and Discussion

3.1 FWM efficiency and bandwidth in AlGaAsOI nano-waveguides

We performed a continuous-wave (CW)-FWM measurement using a pump-probe setup (see Supporting Information). Figure 2a shows the measured FWM spectrum at the output of a 3-mm long AlGaAsOI nano-waveguide with a cross-sectional dimension of 280×640 nm^2. A conversion efficiency of −4.2 dB is obtained when a pump power of 400 mW is coupled in the nano-waveguide. The conversion efficiency has a slightly lower value than expected at pump power larger than 200 mW. Since the effects of three-photon absorption are negligible at this power level (see Supporting Information), the effects of surface states may play a role here and need to be suppressed for higher power operations.[37] Figure 2b shows the measured conversion efficiency as a function of the coupled pump power where the conversion efficiency follows a quadratic relation with the pump power. The solid line shows the fitting from which an effective nonlinearity of 630 $W^{-1}m^{-1}$ is derived. Thanks to the high device nonlinearity, we obtain a higher conversion efficiency than that

reported for conventional (deep-etched) AlGaAs waveguides,[33] and we use only half of the pump power and one-eighth of the device length.

To achieve broadband FWM, the phase matching condition needs to be ensured for a large pump-to-signal detuning. Only a small pump-to-signal detuning was applied in the characterization above to ensure phase-matching. Considering both the linear and nonlinear phase mismatch contributions, the phase mismatch can be expressed as $\kappa=\Delta\beta+2\gamma P_p$, where $\Delta\beta=\beta_s+\beta_i-2\beta_p$ is the linear phase mismatch due to dispersion, β_s, β_i, and β_p are the propagation constants of the signal, idler and pump, respectively. The power dependent nonlinear phase mismatch is due to self-phase modulation (SPM) and cross phase modulation. P_p is the pump power and γ the waveguide effective nonlinearity. In the undepleted pump regime,[38] the output FWM conversion efficiency can be expressed as $\gamma^2 P_p^2 L_{eff}^2 \eta$, where $L_{eff}=(1-e^{-\alpha L})/\alpha$ is the effective length of the waveguide (α: the loss per unit length, L: the waveguide length) and the phase matching factor η can be expressed by the equation

$$\eta=\alpha^2(1+4e^{-\alpha L}\sin^2(\Delta\beta L/2)/(1-e^{-\alpha L})^2)/(\alpha^2+\Delta\beta^2) \quad (1)$$

An efficient parametric conversion occurs when the linear phase mismatch $\Delta\beta$ is close to zero, and such a near-phase-matching condition typically results in a continuous conversion bandwidth centered at the pump frequency. At moderate pump powers ($2\gamma P_p L \ll \pi$), the phase mismatch is mainly dependent on the linear term, which is typically dominated by the second order dispersion β_2 (or group velocity dispersion (GVD) $D=-2\pi c\beta_2/\lambda^2$). Therefore, it is of utmost importance for parametric conversion that the device dispersion can be controlled in an efficient way so that the pump can be placed close to the zero dispersion wavelength (ZDW) to enhance the bandwidth of the continuous main-phase-matched conversion in the vicinity of the pump wavelength. Owing to strong light confinement, the intrinsic normal dispersion of the AlGaAs material can be readily compensated by the waveguide dispersion to be anomalous, and the ZDW can be tuned as shown in Figure 2c. The overall dispersion shape can also be tailored by changing the waveguide cross-sectional dimension.

Enabled by state-of-the-art nano-lithography techniques, the waveguide dimension can be controlled with a sub-10 nm accuracy allowing precise control of dispersion. Focused on lowering and flattening the second order dispersion or GVD, conventional dispersion engineering can also be realized by tailoring the waveguide shape,[6] adding thin over-cladding films,[39] or applying slot waveguide layouts.[40] Here we present a different scheme utilizing high-order phase matching to enhance the continuous bandwidth for strip waveguides in the presence of an ultra-high effective nonlinearity in the device.

Figure 2d shows the measured FWM conversion efficiencies (normalized) as a function of signal-idler wavelength separation (conversion bandwidth) for 3-mm long AlGaAsOI nano-waveguides with different cross-sectional dimensions. We pump the nano-waveguides in the telecom C-band (the pump wavelengths are denoted by the dots in Figure 2c). The pump power is kept at 20 mW at the output of the tapered fiber. In spite of a relatively large GVD value (670 ps/km/nm) at the pump wavelength, the nano-waveguide with a cross-sectional dimension of 305×500 nm^2 exhibits a broad conversion bandwidth of 100 nm due to the short waveguide length. While taking into account the high-order phase matching, the dispersion engineered cross-sectional dimension (280×640 nm^2) allows for an ultra-broad conversion bandwidth of about 750 nm, which not only covers the telecom O-band to U-band, but also offers access to the 2-μm wavelength region where new fibers and amplifiers are developed for future ultra-high-capacity communications networks.[41]

Considering higher dispersion orders of the waveguide and assuming that dispersion orders only up to β_5 are significant, the linear phase mismatch $\Delta\beta$ can be approximated as $\beta_4\Delta\omega^4/12+\beta_2\Delta\omega^2$, where $\Delta\omega=\omega_s-\omega_p$ is the angular frequency separation between the signal and the pump, and β_4 is the fourth order dispersion coefficient. If $\beta_2\beta_4<0$, phase matching also occurs for $\Delta\omega = \pm\sqrt{-12\beta_2/\beta_4}$, which gives rise to a discrete high-order phase-matched conversion band on top of the main phase-matched conversion band. This conversion behavior has been demonstrated with ultra-large pump-signal

frequency separation,[42] and has been proposed as a means to realize light sources at otherwise unattainable wavelength ranges.[43] However, the discrete conversion band is normally very narrow and has little impact on the optimal pumping wavelength and the bandwidth of the main phase-matched conversion band. If the device nonlinearity can be made sufficiently high so that the interaction length can be significantly reduced while maintaining high efficiency, the overall conversion bandwidth becomes sensitive to the high-order dispersion. Figure 2e shows the simulated phase-mismatch ($|\Delta\beta \cdot L/\pi|$) for different pump and signal wavelength settings for a 3-mm long AlGaAsOI device with a waveguide dimension of 280×640 nm^2. The solid lines correspond to the boundaries of the near-phase-matched conversion, where the conversion efficiency is half that of the perfect-phase-matched case. Compared to pumping at the ZDW (about 1540 nm), a significant bandwidth enhancement can be obtained by carefully choosing the pump wavelength according to the higher order phase-matching conditions. Depending on the device length, the optimal pump wavelength moves away from the ZDW leading to a merger of the main phase-matched conversion band and the high-order phase-matched conversion bands realizing an ultra-broad continuous "synergetic" conversion band. Though waveguide dispersion is sensitive to any small dimension change due to fabrication imperfections, especially for high confinement waveguides, the high-order phase-matched waveguide can be readily realized using state-of-the-art patterning technologies (see Supporting Information). Figure 2f shows the simulated conversion efficiency (normalized) evolution as the waveguide length increases when the nano-waveguide is pumped at 1560 nm. It is seen that the "synergetic" conversion band is present as long as the waveguide length is kept within three millimeters as the strict phase matching requirement between those bands is relaxed for such a compact device. While it is the high index contrast that enables the broad bandwidth it is the high effective nonlinearity that allows a short device and makes the scheme interesting in practice.

3.2 FWM performance comparison of nonlinear waveguides in different material platforms

Figure 3 summarizes the CW-FWM performances concerning the achieved maximum conversion efficiency and continuous bandwidth for nonlinear waveguides reported in different material platforms. The color of the data points is scaled according to the waveguide effective nonlinearity. Pioneering work on CW-FWM in integrated platforms starts with the SOI waveguide platform. M.A. Foster at al. demonstrated a broadband FWM operation (~150 nm) in a silicon strip waveguide.[5] Limited by the TPA-induced FCA, the FWM conversion efficiency saturated at −10 dB. An ultra-broad FWM conversion bandwidth has been demonstrated in silicon waveguides with a thin slab layer.[6] However, due to a longer carrier lifetime, the conversion efficiency saturated at a lower level (−18 dB). To mitigate the FCA effects, a reverse-biased p-i-n diode has been employed in a silicon rib waveguide to remove the generated carriers, which pushed the conversion efficiency to −1 dB.[7] The conversion bandwidth is, however, limited by the reduced freedom to dispersion engineer for such a waveguide layout. It is very challenging to simultaneously achieve optimal conversion efficiency and bandwidth in the SOI platform. As shown in Figure 3, the achieved results in the SOI platform follows the dashed gray line, which shows a constant efficiency-bandwidth product.

In the last decade, tremendous efforts have been made to develop the ultimate material platform with a higher FOM that can outperform the SOI platform for nonlinear parametric processes. Engineering silicon-based materials like silicon ultra-rich nitride (Si_7N_3),[18] amorphous silicon (a-Si),[19] silicon germanium ($Si_{1-x}Ge_x$),[20] and silicon nano-crystal (Si-nc)[23] can enhance the device nonlinearity. However, the increased TPA coefficient also limits the FWM performance for $Si_{1-x}Ge_x$ and a-Si (in the case of pushing material nonlinearity[44]) while the extra material absorption associated with the material engineering also limit the performance in the case of $Si_{1-x}Ge_x$, Si_7N_3, and Si-nc. To avoid the detrimental TPA, materials with lower refractive index than silicon but larger bandgaps including tantalum pentoxide (Ta_2O_5),[12] silicon carbide (SiC),[15] silicon (rich)

nitride (S_xN_y),[21] Si_3N_4,[45] and chalcogenides (ChG)[46] have been investigated. Though low loss waveguides are realized in those materials enabling a long nonlinear interaction, the demonstrated conversion efficiencies are limited at a lower level even with high pump powers due to an order of magnitude lower device nonlinearities than the aforementioned silicon-based materials. The achieved bandwidths are also limited due to the unavoidable phase mismatch induced by a long waveguide length. Though SiC exhibits a relatively good performance among those TPA-free materials, the overall performance is limited due to the intrinsic material absorption and immature fabrication technology at present. It is clear that the material platforms with higher effective nonlinearities find their places in the upper right region (higher efficiency-bandwidth product region) in Figure 3.

III-V materials such as AlGaAs and InGaP both exhibit large material inherent nonlinearities and large bandgaps. Without the nonlinear loss limit from TPA, a conversion efficiency as high as −6 dB has been demonstrated in a 2.5-centimeter-long conventional AlGaAs waveguide[33]. However, the low-index contrast waveguide layout makes the dispersion engineering challenging for the realization of broadband operation. Using high-index-contrast waveguide layout, one can take full advantage of the high intrinsic nonlinearity of a nonlinear medium and also enable efficient dispersion engineering. Although attempts on the InGaP-on-insulator platform result in a similar high device nonlinearity[16] as AlGaAsOI, the large linear loss induced by the current fabrication technology severely limits its performance. Therefore, only by combining a high material quality, a high material nonlinearity, high waveguide confinement, a sophisticated dispersion design and mature fabrication technology, a CW-FWM performance superior to that of the SOI platform can be achieved. This is demonstrated in the AlGaAsOI platform in this work, where we show a -4 dB conversion efficiency and a 750 nm conversion bandwidth, upper right corner of Figure 3.

3.3 System demonstration of all-optical wavelength conversion beyond a terabaud

As a suitably challenging OSP application, which would need to take advantage of both the FWM efficiency and the ultra-broadband nature offered by the AlGaAOI platform, we performed wavelength conversion of an ultra-high speed data signal, which consists of a train of sub-ps pulses and spectrally almost covers the whole C-band. The experimental setup for the wavelength conversion of a 1.28−Tbit/s serial return-to-zero (RZ) DPSK signal is shown in Figure 4a. In the 1.28−Tbit/s transmitter, a 10-GHz pulse train is generated from a mode-locked laser and then compressed by SPM and dispersion. The generated short pulses are DPSK modulated by a 10−Gbit/s FEC (6.6% overhead) coded data pattern in a Mach-Zehnder modulator (MZM). The modulated 10−Gbit/s DPSK signal is multiplexed in time to 1.28 Tbit/s using a passive fiber-delay multiplexer (MUX ×128). The generated 1.28-Tbit/s RZ-DPSK signal at 1550 nm is combined with a CW pump at 1568 nm through a WDM coupler and launched into the AlGaAsOI nano-waveguide. Both the pump and the signal waves are aligned to the TE polarization of the AlGaAsOI nano-waveguide. The input pump power is kept at 35.5 mW to ensure good fiber-to-chip alignment stability. Figure 4b shows the optical spectra at the input (green for the pump and blue for the signal) and the output (black curve) of the nano-waveguide. The wavelength-converted signal centered at 1586 nm is extracted from the pump and the original signal using a filtering subsystem, consisting of optical bandpass filters and an EDFA in between (see red curve in Figure 4b). The wavelength-converted signal is characterized in the time domain by measuring autocorrelation traces (Figure 4c). The pulse width (FWHM: 340 fs) of the wavelength-converted data pulses is almost unchanged compared to the input data pulses (FWHM: 350 fs) as a benefit of an abundant conversion bandwidth. The converted 1.28−Tbit/s OTDM signal is received by a 1.28−Tbit/s time-domain optical Fourier transformation (TD-OFT) based OTDM receiver,[47] and the de-multiplexed 10 Gbit/s channels are detected by a 10 Gbit/s DPSK receiver, and finally decoded by a FEC decoder. The performance of

the converted signal is evaluated by error counting before and after FEC decoding. Figure 4d shows the BER measurements before the FEC decoding for both the back-to-back 1.28 Tbit/s signal and the converted 1.28 Tbit/s signal. The inset of Figure 4e shows the 10 Gbit/s demultiplexed and demodulated eye diagram from the 1.28 Tbit/s wavelength converted RZ-DPSK signal. The wavelength-converted 1.28−Tbit/s RZ-DPSK signal achieves a BER well below the FEC limit of 3×10^{-3} for all 128 tributaries as shown in Figure 4f (upper). The wavelength conversion experiment is performed at moderate pump power (minimum to achieve a proper conversion), which limits the conversion efficiency to −23 dB. Therefore, the optical signal-to-noise ratio (OSNR) of the signal degrades after the conversion, resulting in an error floor at BER~10^{-5}. The error floor could be lowered if the conversion efficiency is increased by increasing the pump power. We also measure the absolute post-FEC errors (Figure 4f (lower)). The FEC module properly corrects the errors to yield zero errors for all 128 demultiplexed 10−Gbit/s channels of the wavelength-converted signal. This corresponds to a post-FEC error-free performance at a net data rate of 1.2 Tbit/s.

Compared to a previous demonstration of wavelength conversion of a 640 Gbit/s data signal in a silicon waveguide[4] with slightly worse performance, the required pump power used in this experiment is much less even though the data rate is doubled thanks to the ultra-high device nonlinearity of the AlGaAsOI nano-waveguide. Using the same pump power, the BER measurement of wavelength conversion of 640 Gbit/s data in an AlGaAsOI nano-waveguide shows an error-free performance at 10^{-9} without using FEC module (see Supporting Information). Very recently, I. Sackey et al. demonstrated 1.024 Tbit/s wavelength conversion in a silicon rib waveguide with a p−i−n diode where the eight parallel 16QAM data signals are processed at a symbol rate of 32 Gbauds.[48] In our work, we convert a serial 1.28 Tbaud single channel single polarization data signal carrying binary data resulting in 1.28 Terabit/s, thus clearly validating the ultra-fast nature of the nonlinear parametric process.

3.4 FWM in AlGaAsOI microresonators

To further reduce the power consumption, resonance effects in resonant waveguides like PhCWs or microresonators can be utilized to enhance the FWM conversion efficiency. In PhCWs, the enhancement is enabled by slowing down the light propagation in nonlinear media. However, the operation wavelength ranges of such slow-light PhCWs are very narrow (typically less than 15 nm) even for optimized designs.[24] In microresonators, the enhancement is realized due to a high intracavity circulating power,[25] and the conversion efficiency can be expressed by $\gamma^2 P_p^2 L_{eff}^2 FE_p^4 FE_s^2 FE_i^2$. In the phase-matching case, FE_k (k=p,s,i corresponds to pump, signal, and idler, respectively) is the field enhancement factor estimated by $\kappa/(1-a\tau)$, where κ, τ, and a are the coupling coefficient, transmission coefficient, and the amplitude transmission coefficient, respectively.[25] The maximum *FE* can be achieved at the critical coupling condition (κ=a). Parametric amplification and oscillation can be obtained under CW pumping operation for high quality-factor (*Q)* microresonators,[9,10,34] which can be potentially utilized as multi-wavelength light sources for WDM systems.[49] Though the overall wavelength operation range for the parametric operations in microresonators can be very broad (up to an octave span), the narrow resonance linewidth of such high *Q* microresonators limits their capability to handle high-repetition-rate data signals carried by optical pulses with broad spectra. The filtering induced pulse broadening in those narrow-linewidth devices may lead to a crosstalk between neighboring pulses. A moderate *Q* microresonator is therefore more suitable for OSP applications in spite of a reduced *FE* factor. The overall wavelength conversion performance for microresonators in OSP is always a trade-off between the *FE* factor and operation linewidth (see Supporting Information). Compared with straight waveguides, the power consumption can be significantly reduced in microresonators at the price of a reduced maximal data rate for single-channel wavelength conversion. However, the data rate limitation can be mitigated to some extent by using a more sophisticated design such as the coupled

resonator optical waveguide (CROW) design[26] where low Q microresonators with wider operation linewidths can be used while maintaining a high FE factor, due to a further reduced group velocity at resonance wavelengths. Since the main building block of a CROW design is a single resonator, we focus our discussion on single microresonators in this section.

Figure 5a shows a fabricated 17.2-μm-radius AlGaAsOI microresonator with a free spectral range (FSR) of 730 GHz. The device is designed to be operated under over-coupled conditions for a relatively broad resonance linewidth. Figure 5b presents the measured (normalized) transmission spectrum of the microresonator. The resonance linewidth of the resonator is around 35 pm, which corresponds to 4.5 GHz (the loaded Q factor is around 44,000). Figure 5c shows the spectra of the input pump (green) and the signal (blue) when their wavelengths are off-resonance. The black curve shows the output spectrum when both pump and signal are on-resonance. With a coupled pump power of only 250 μW, an idler is observed, and conversion efficiency (output idler power/input signal power) of −40 dB is obtained. Figure 5d shows the measured conversion efficiency as a function of the coupled pump power in the bus waveguide and a maximum net efficiency of −12 dB is obtained with only 7 mW pump power. Compared to FWM in a straight waveguide with the same physical device length, we obtain a 53 dB enhancement of the FWM conversion efficiency (see Supporting Information).

3.5 FWM performance comparison for microresonators in different platforms

Since the first demonstration of FWM-based wavelength conversion in GaAs microresonator using a pulsed pump,[25] several different material platforms have been explored to push the performance for microresonator-based wavelength conversion under CW operation.[26–31] Ideally, a microresonator should have a large resonance linewidth but allow a high conversion efficiency at a low pump power. Figure 6a summarizes CW-FWM performances of microresonators made in different material platforms concerning the conversion efficiency, the resonator linewidth and the

power consumption. The color of the data points is scaled as the pump power used in the corresponding demonstrations. For low-index contrast Hydex microresonators, either a narrow linewidth is required to enable a low-power conversion[27], and a high pump power (>100 mW) is required to achieve an efficient conversion for broad-linewidth devices.[28] Most of the demonstrated conversion efficiencies are below −25 dB. The TPA-induced FCA is still the main detrimental effect that limits the performance of silicon devices.[29] There is a recent attempt to further enhance the nonlinearity by adding a highly nonlinear graphene top thin layer. However, the reduced Q of the microresonator due to the lossy properties of graphene suppresses the effective nonlinearity enhancement.[30] Although efforts have made been made to take advantage of a high intrinsic nonlinearity in conventional deep-etched AlGaAs waveguides, the achieved conversion efficiency is fairly low (less than −40 dB) due to the challenging fabrication, especially in patterning the bus-to-ring coupling gap for microresonators.[31] It is seen that for the GHz resonance linewidth, the achieved conversion efficiency in the AlGaAsOI is the highest and with the lowest coupled pump power. It is worth noting that although the demonstrated efficiency in SOI for the CROW design is relatively low in [26], the conversion efficiency is enhanced by 28 dB compared with a single microresonator device made on the same chip. Therefore, the CROW scheme can be utilized to further improve the performance of the AlGaAsOI microresonator devices. Alternatively, "photonic molecule"-like coupled-cavity system design can be used to engineer different modes for optimum FWM performance independently.[50]

In order to compare the CW-FWM performance of microresonators made by different emerging TPA-free platforms[9–18], as listed in Table 1, we calculate the relative conversion efficiency as a function of the resonance linewidth for microresonators in Figure 6b. Here, the FSR of the microresonators is assumed to be the same as that of the AlGaAsOI device used in Figure 5. The operating linewidth for the maximum conversion efficiency is mainly dependent on the linear loss of

the waveguide (or the *FE* factor) while the achievable maximum conversion efficiency is dependent on the device nonlinearity. The device nonlinearity becomes a dominant effect for the performance for larger operating linewidths as the *FE* factor reduces dramatically in the GHz linewidth range. For instance, InGaP outperforms Hydex and diamond at an operating linewidth larger than 10 GHz in spite of an order of magnitude larger linear loss. Therefore, to choose a platform for the OSP applications using microresonators, nonlinearity should be the main concern since the linear loss has limited impact on devices with GHz resonance linewidth. For a certain material platform, it is, therefore, more important to engineer the waveguide to enhance the light confinement (the effective nonlinearity) than to reduce the linear loss – this is in contrast to recent efforts to lower the linear loss by using larger cross-section dimension waveguides of microresonators for frequency comb generation.[51] It is seen that the AlGaAsOI platform exhibit the best performance for GHz-linewidth microresonators because of an ultra-high material nonlinearity and a relatively low linear loss benefit from well-developed fabrication technologies.

To further improve the performance of AlGaAsOI microresonators, the sidewall roughness-induced scattering and surface state effects need to be suppressed, and optimized coupler design should be exploited (see Supporting Information). To make AlGaAs devices more versatile, electro-optic or thermo-optic effects can be utilized to realize device tunability while heterogeneous integration technologies can be used to bridge between the ultra-high nonlinearities of AlGaAs and CMOS compatible platforms.[52]

4. Conclusion

We have realized an ultra-efficient nonlinear AlGaAsOI waveguide platform showing the highest FOM among planar integrated nonlinear platforms. Leveraging the ultra-high nonlinearity of the AlGaAsOI nano-waveguide, we have achieved a CW-FWM conversion efficiency of −4 dB in a 3-mm-long device. We have also presented a new scheme to generate an ultra-broad continuous

synergetic conversion band and realized a 750-nm bandwidth by optimizing the dispersion considering high-order phase-matching and carefully choosing the pump wavelength. This demonstrated scheme can be employed as a universal dispersion engineering scheme for other highly nonlinear material platforms such as a-Si, Si_7N_3, and InGaP to obtain ultra-broadband frequency conversion, which will be potentially valuable for telecommunication, microscopy, spectroscopy, quantum optics, and optical frequency metrology. We have also successfully pushed the demonstrated speed for all-optical wavelength conversion of single-polarization serial data signals beyond terabaud, which shows great potentials for the AlGaAsOI waveguide platform for ultra-fast OSP. Moreover, we have shown that the power consumption of such wavelength conversion can be significantly reduced by using an AlGaAsOI microresonator. A conversion efficiency of −12 dB has been obtained by employing a CW-pump power of only 7 mW for a GHz-linewidth device. With the advent of on-chip lasers and hybrid fabrication technologies,[53] an ultra-compact, fully-integrated ultra-low power wavelength converter can be envisioned utilizing the high-confinement AlGaAsOI waveguide platform in the future.

Acknowledgment

The authors acknowledge support from the DNRF Research Centre of Excellence, SPOC (DNRF123), and the Villum Foundation's Centre of Excellence, NATEC II. The authors thank Kjeld Dalgaard for assistance in device characterization.

Received: ((will be filled in by the editorial staff))
Revised: ((will be filled in by the editorial staff))
Published online: ((will be filled in by the editorial staff))

Keywords

Optical signal processing, four-wave mixing, all-optical wavelength conversion, integrated nonlinear optics, third-order nonlinear material

References

[1] D. Cotter, R. J. Manning, K. J. Blow, A. D. Ellis, A. E. Kelly, D. Nesset, I. D. Phillips, A. J. Poustie, and D. C. Rogers, *Science* **286** 1523–1528 (1999).

[2] T. Torounidis, P. A. Andrekson, and B. E. Olsson, *IEEE Photonics Technol. Lett.* **18** 1194–1196 (2006).

[3] J. Leuthold, C. Koos, and W. Freude, *Nat. Photonics* **4** 535–544 (2010).

[4] H. Hu, H. Ji, M. Galili, M. Pu, C. Peucheret, H. C. H. Mulvad, K. Yvind, J. M. Hvam, P. Jeppesen, and L. K. Oxenløwe, *Opt. Express* **19** 19886 (2011).

[5] M. A. Foster, A. C. Turner, R. Salem, M. Lipson, and A. L. Gaeta, *Opt. Express* **15** 12949 (2007).

[6] A. C. Turner-Foster, M. A. Foster, R. Salem, A. L. Gaeta, and M. Lipson, *Opt. Express* **18** 1904 (2010).

[7] A. Gajda, L. Zimmermann, M. Jazayerifar, G. Winzer, H. Tian, R. Elschner, T. Richter, C. Schubert, B. Tillack, and K. Petermann, *Opt. Express* **20** 13100 (2012).

[8] M. E. Marhic, P. A. Andrekson, P. Petropoulos, S. Radic, C. Peucheret, and M. Jazayerifar, *Laser Photon. Rev.* **9** 50–74 (2015).

[9] L. Razzari, D. Duchesne, M. Ferrera, R. Morandotti, S. Chu, B. E. Little, and D. J. Moss, *Nat. Photonics* **4** 41–45 (2009).

[10] J. S. Levy, A. Gondarenko, M. a. Foster, A. C. Turner-Foster, A. L. Gaeta, and M. Lipson, *Nat. Photonics* **4** 37–40 (2009).

[11] H. Jung, C. Xiong, K. Y. Fong, X. Zhang, and H. X. Tang, *Opt. Lett.* **38** 2810–3 (2013).

[12] C.-L. Wu, Y.-J. Chiu, C.-L. Chen, Y.-Y. Lin, A.-K. Chu, and C.-K. Lee, *Opt. Lett.* **40** 4528 (2015).

[13] B. J. M. Hausmann, I. Bulu, V. Venkataraman, P. Deotare, and M. Lončar, *Nat. Photonics* **8**

369–374 (2014).

[14] C. C. Evans, K. Shtyrkova, J. D. B. Bradley, O. Reshef, E. Ippen, and E. Mazur, *Opt. Express* **21** 18582 (2013).

[15] J. Cardenas, S. Miller, Y. Okawachi, S. Ramelow, A. G. Griffith, A. Farsi, A. L. Gaeta, and M. Lipson, in *Conference on Lasers and Electro-Optics (CLEO)*, 2015, SF1D.7.

[16] U. D. Dave, B. Kuyken, F. Leo, S.-P. Gorza, S. Combrie, A. De Rossi, F. Raineri, and G. Roelkens, *Opt. Express* **23** 4650 (2015).

[17] C. Lacava, S. Stankovic, A. Z. Khokhar, T. D. Bucio, F. Y. Gardes, G. T. Reed, D. J. Richardson, and P. Petropoulos, *Sci. Rep.* **7** 22 (2017).

[18] K. J. A. Ooi, D. K. T. Ng, T. Wang, A. K. L. Chee, S. K. Ng, Q. Wang, L. K. Ang, A. M. Agarwal, L. C. Kimerling, and D. T. H. Tan, *Nat. Commun.* **8** 13878 (2017).

[19] K.-Y. Wang and A. C. Foster, *Opt. Lett.* **37** 1331 (2012).

[20] M. A. Ettabib, C. Lacava, Z. Liu, A. Bogris, A. Kapsalis, M. Brun, P. Labeye, S. Nicoletti, D. Syvridis, D. J. Richardson, and P. Petropoulos, *Opt. Express* **25** 3252 (2017).

[21] C. J. Krückel, A. Fülöp, T. Klintberg, J. Bengtsson, P. A. Andrekson, and V. Torres-Company, *Opt. Express* **23** 25827 (2015).

[22] C. Koos, P. Vorreau, T. Vallaitis, P. Dumon, W. Bogaerts, R. Baets, B. Esembeson, I. Biaggio, T. Michinobu, F. Diederich, W. Freude, and J. Leuthold, *Nat. Photonics* **3** 216–219 (2009).

[23] A. Trita, C. Lacava, P. Minzioni, J. P. Colonna, P. Gautier, J. M. Fedeli, and I. Cristiani, *Appl. Phys. Lett.* **99** 1–4 (2011).

[24] J. Li, L. O'Faolain, I. H. Rey, T. F. Krauss, L. O'Faolain, I. H. Rey, and T. F. Krauss, *Opt. Express* **19** 4458–4463 (2011).

[25] P. P. Absil, J. V Hryniewicz, B. E. Little, P. S. Cho, R. a Wilson, L. G. Joneckis, and P. T.

Ho, *Opt. Lett.* **25** 554–6 (2000).

[26] F. Morichetti, A. Canciamilla, C. Ferrari, A. Samarelli, M. Sorel, and A. Melloni, *Nat. Commun.* **2** 296 (2011).

[27] M. Ferrera, D. Duchesne, L. Razzari, M. Peccianti, R. Morandotti, P. Cheben, S. Janz, D.-X. Xu, B. E. Little, S. Chu, and D. J. Moss, *Opt. Express* **17** 14098–103 (2009).

[28] A. Pasquazi, R. Ahmad, M. Rochette, M. Lamont, B. E. Little, S. T. Chu, R. Morandotti, and D. J. Moss, *Opt. Express* **18** 3858 (2010).

[29] A. C. Turner, M. a Foster, A. L. Gaeta, and M. Lipson, *Opt. Express* **16** 4881–7 (2008).

[30] X. Hu, Y. Long, M. Ji, A. Wang, L. Zhu, Z. Ruan, Y. Wang, and J. Wang, *Opt. Express* **24** 7168 (2016).

[31] P. Kultavewuti, V. Pusino, M. Sorel, and J. Stewart Aitchison, *Opt. Lett.* **40** 3029 (2015).

[32] G. I. Stegeman, A. Villeneuve, J. Kang, J. S. Aitchison, C. N. Ironside, K. Al-Hemyari, C. C. Yang, C.-H. Lin, H.-H. Lin, G. T. Kennedy, R. S. Grant, and W. Sibbett, *J. Nonlinear Opt. Phys. Mater.* **03** 347–371 (1994).

[33] J. J. Wathen, P. Apiratikul, C. J. K. Richardson, G. A. Porkolab, G. M. Carter, and T. E. Murphy, *Opt. Lett.* **39** 3161–4 (2014).

[34] M. Pu, L. Ottaviano, E. Semenova, and K. Yvind, *Optica* **3** 823 (2016).

[35] N. Morais, I. Roland, M. Ravaro, W. Hease, A. Lemaître, C. Gomez, S. Wabnitz, M. De Rosa, I. Favero, and G. Leo, *Opt. Lett.* **42** 4287 (2017).

[36] L. Ottaviano, M. Pu, E. Semenova, and K. Yvind, *Opt. Lett.* **41** 3996 (2016).

[37] S. Grillanda and F. Morichetti, *Nat. Commun.* **6** 8182 (2015).

[38] R. W. Tkach, A. R. Chraplyvy, F. Forghieri, A. H. Gnauck, and R. M. Derosier, *J. Light. Technol.* **13** 841–849 (1995).

[39] X. Liu, W. M. J. Green, X. Chen, I.-W. Hsieh, J. I. Dadap, Y. A. Vlasov, and R. M. Osgood,

Jr., *Opt. Lett.* **33** 2889 (2008).

[40] L. Zhang, Y. Yue, R. G. Beausoleil, and A. E. Willner, *Opt. Express* **18** 20529–20534 (2010).

[41] H. Zhang, N. Kavanagh, Z. Li, J. Zhao, N. Ye, Y. Chen, N. V. Wheeler, J. P. Wooler, J. R. Hayes, S. R. Sandoghchi, F. Poletti, M. N. Petrovich, S. U. Alam, R. Phelan, J. O'Carroll, B. Kelly, L. Grüner-Nielsen, D. J. Richardson, B. Corbett, and F. C. Garcia Gunning, *Opt. Express* **23** 4946 (2015).

[42] X. Liu, B. Kuyken, G. Roelkens, R. Baets, R. M. Osgood, and W. M. J. Green, *Nat. Photonics* **6** 667–671 (2012).

[43] E.-K. Tien, Y. Huang, S. Gao, Q. Song, F. Qian, S. K. Kalyoncu, and O. Boyraz, *Opt. Express* **18** 21981 (2010).

[44] K. Narayanan and S. F. Preble, *Opt. Express* **18** 8998 (2010).

[45] C. J. Krückel, V. Torres-Company, P. A. Andrekson, D. T. Spencer, J. F. Bauters, M. J. R. Heck, and J. E. Bowers, *Opt. Lett.* **40** 875 (2015).

[46] M. D. Pelusi, F. Luan, S. Madden, D.-Y. Choi, D. A. Bulla, B. Luther-Davies, and B. J. Eggleton, *IEEE Photonics Technol. Lett.* **22** 3–5 (2010).

[47] H. C. Hansen Mulvad, E. Palushani, H. Hu, H. Ji, M. Lillieholm, M. Galili, A. T. Clausen, M. Pu, K. Yvind, J. M. Hvam, P. Jeppesen, and L. K. OxenlØwe, *Opt. Express* **19** (2011).

[48] I. Sackey, A. Gajda, A. Peczek, E. Liebig, L. Zimmermann, K. Petermann, and C. Schubert, *Opt. Express* **25** 21229 (2017).

[49] P. Marin-Palomo, J. N. Kemal, M. Karpov, A. Kordts, J. Pfeifle, M. H. P. Pfeiffer, P. Trocha, S. Wolf, V. Brasch, M. H. Anderson, R. Rosenberger, K. Vijayan, W. Freude, T. J. Kippenberg, and C. Koos, *Nature* **546** 274–279 (2017).

[50] X. Zeng and M. A. Popović, *Opt. Express* **22** 15837 (2014).

[51] X. Ji, F. A. S. Barbosa, S. P. Roberts, A. Dutt, J. Cardenas, Y. Okawachi, A. Bryant, A. L. Gaeta, and M. Lipson, *Optica* **4** 619 (2017).

[52] H. El Dirani, C. Sciancalepore, C. Monat, X. Letartre, S. Brision, C. Jany, N. Olivier, K. Yvind, E. Semenova, L. Katsuo Oxenløwe, L. Hagedorn Frandsen, M. Pu, and P. D. Girouard, in *Integrated Optics: Devices, Materials, and Technologies XXII*, 2018, **1053508**, 7.

[53] D. Liang and J. E. Bowers, *Nat. Photonics* **4** 511–517 (2010).

Figures

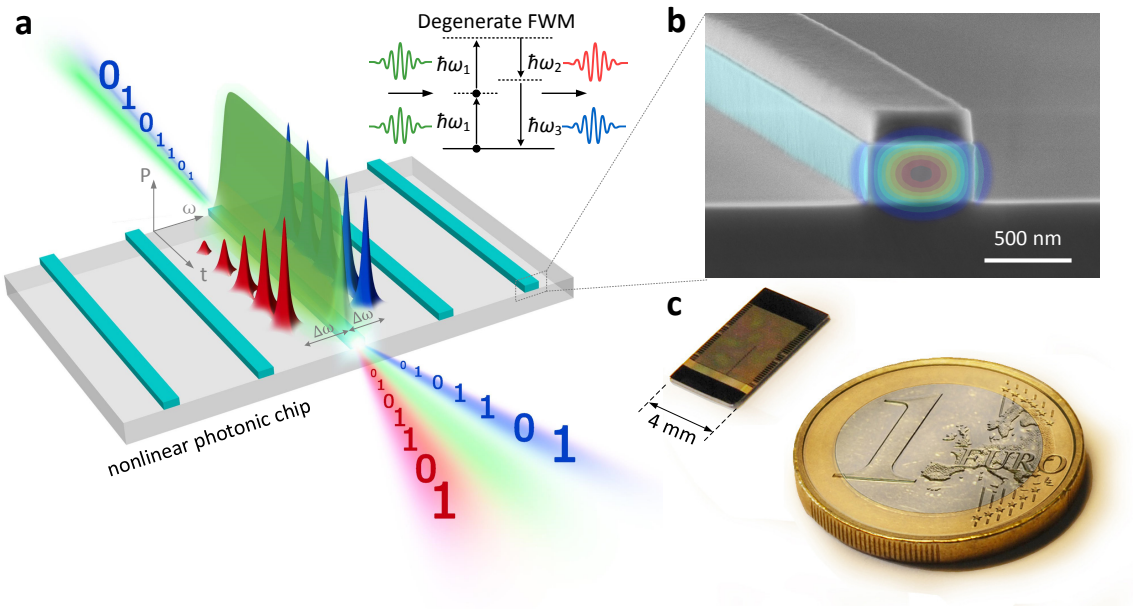

Figure 1 Nonlinear photonic chip for optical signal processing (OSP)

(a) Schematic illustration of an example OSP: all-optical wavelength conversion of data signals based on degenerate four-wave mixing (FWM) in a nonlinear waveguide on a photonic chip.

(b) Scanning electron microscopy (SEM) picture of an AlGaAs-on-insulator (AlGaAsOI) nano-waveguide (denoted by artificial blue color) fabricated by electron-beam lithography and inductive-coupled plasma dry etching process. The top left-over layer is the electron-beam resist which is used as an etching mask for patterning. The simulated field distribution for the fundamental TE mode is superimposed on the image showing strong light confinement.

(c) Photograph of a one euro coin and a fabricated 4-mm-wide AlGaAsOI photonic chip accommodating hundreds of waveguide-based devices.

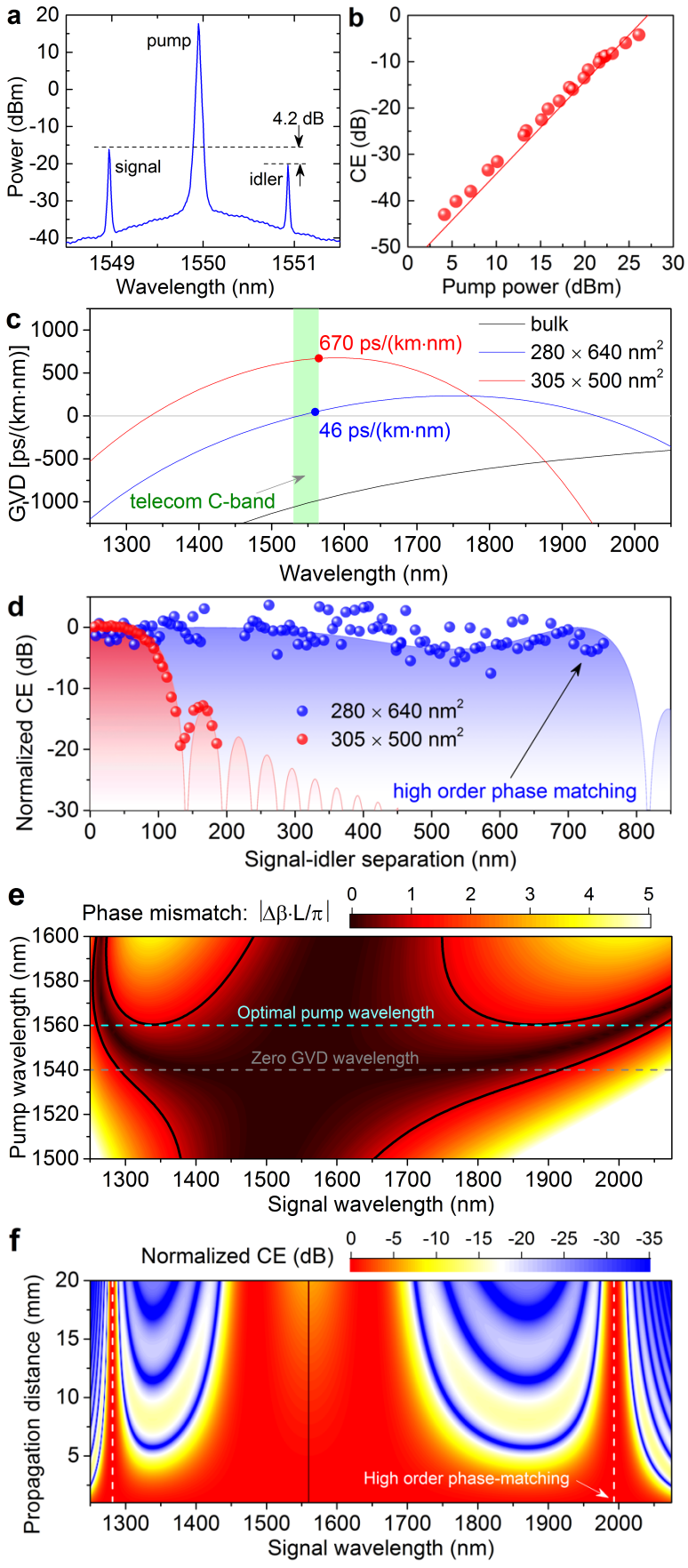
a
Power (dBm)
pump
signal
idler
4.2 dB
Wavelength (nm)
b
CE (dB)
Pump power (dBm)
c
GVD [ps/(km·nm)]
670 ps/(km·nm)
46 ps/(km·nm)
telecom C-band
bulk
280 × 640 nm²
305 × 500 nm²
Wavelength (nm)
d
Normalized CE (dB)
280 × 640 nm²
305 × 500 nm²
high order phase matching
Signal-idler separation (nm)
e
Phase mismatch: |Δβ·L/π|
Pump wavelength (nm)
Optimal pump wavelength
Zero GVD wavelength
Signal wavelength (nm)
f
Normalized CE (dB)
Propagation distance (mm)
High order phase-matching
Signal wavelength (nm)

Figure 2 FWM characterization of AlGaAsOI nano-waveguides

(a) Measured optical output spectrum of a 3-mm-long AlGaAsOI nano-waveguide (cross-sectional dimension: 280×640 nm^2) when a pump wave (1550 nm, 400 mW) and a signal wave (1549 nm, 100 μW) are coupled into the device under continuous-wave (CW) operation.

(b) Measured output FWM conversion efficiency (CE) as a function of pump power for the device. The pump wavelength is set in the telecom C-band.

(c) Calculated group velocity dispersion (GVD) parameter for AlGaAsOI nano-waveguides with different cross-sectional dimensions. The black curve shows the dispersion property for the bulk AlGaAs material.

(d) Measured FWM conversion efficiency (normalized) as a function of signal-idler wavelength separation for different AlGaAsOI nano-waveguides. Solid lines and shaded area show the simulation results.

(e) Calculated phase mismatch $|\Delta\beta \cdot L/\pi|$ for different pump and signal wavelength setting for the 3-mm-long AlGaAsOI nano-waveguide with a cross-sectional dimension of 280×640 nm^2. The black contour line shows the boundaries for the near-phase-matching region ($|\Delta\beta \cdot L/\pi|<1$). The gray and cyan lines correspond to the zero dispersion wavelength and the optimal pump wavelength, respectively.

(f) Calculated conversion efficiency (normalized at each distance) as a function of signal wavelength for different waveguide lengths when the AlGaAsOI nano-waveguide is pumped at 1560 nm. The white dashed lines shows the high-order phase-matched wavelengths.

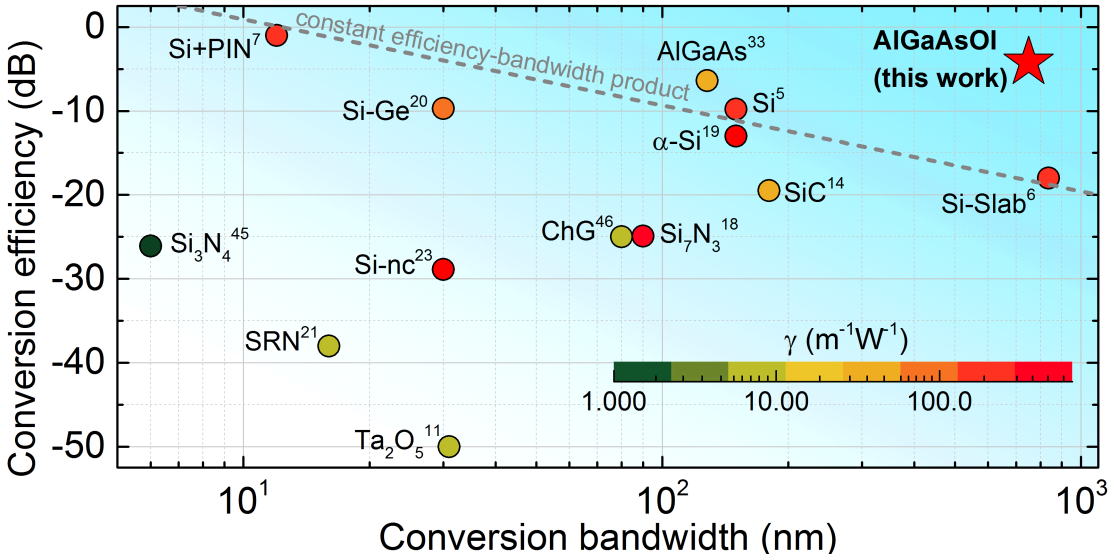

Figure 3 CW-FWM performance comparison

Summary of experimentally achieved conversion efficiency and bandwidth for FWM at telecom wavelengths in straight waveguides in different material platforms. The gray dashed line is used as a guide for the eyes showing a constant efficiency-bandwidth product.

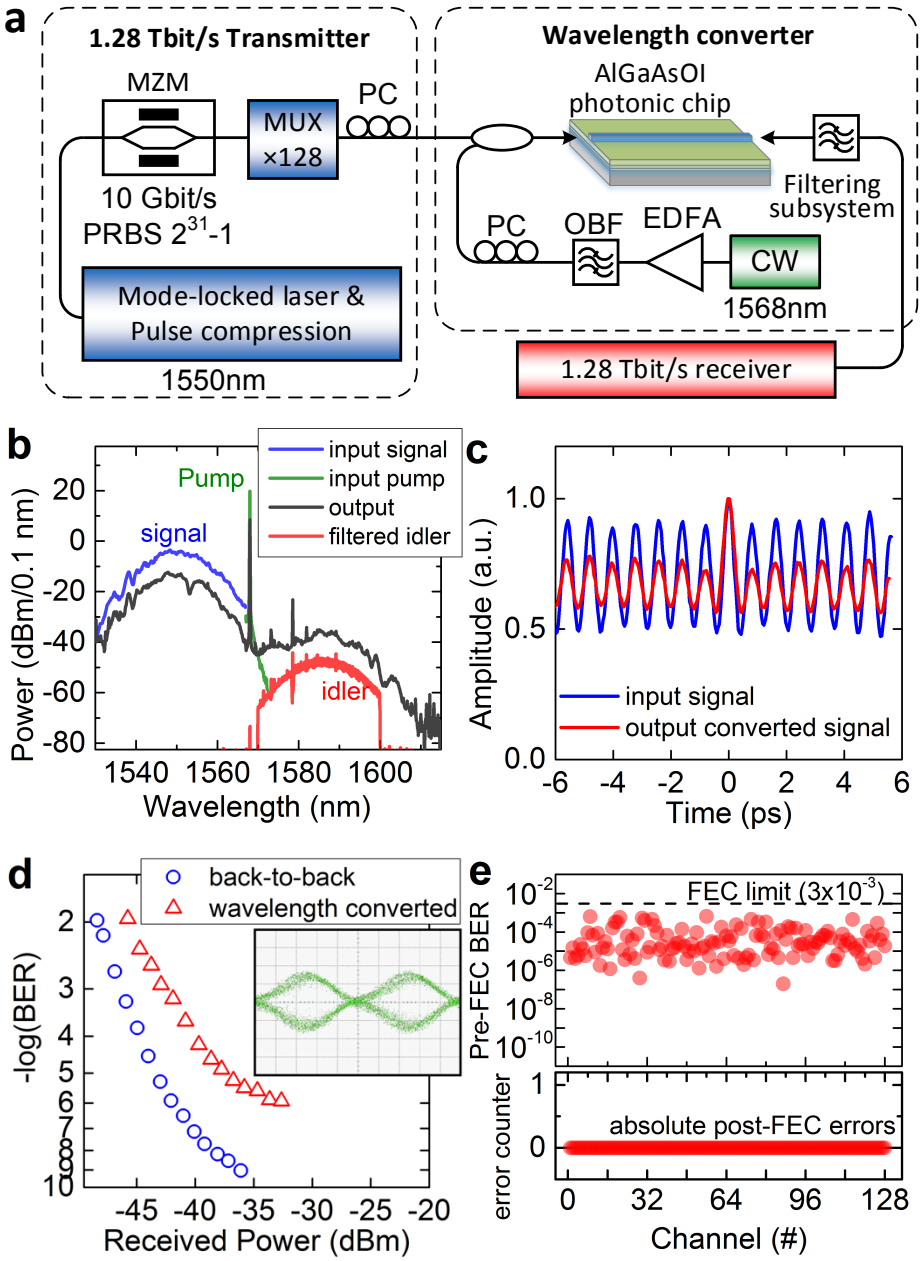

Figure 4 Wavelength conversion experiment

(a) Experimental setup for all-optical wavelength conversion of a 1.28 Tbit/s DPSK data signal.

(b) Spectra at the input, output of the AlGaAsOI nano-waveguide and the converted signal after filtering.

(c) Autocorrelation trace of the input signal and the output converted signal.

(d) BER measurements for the 1.28 Tbit/s back-to-back and the wavelength-converted signal. Inset: eye diagram of a 10 Gbit/s demultiplexed channel from the 1.28 Tbit/s converted signal.

(e) BER for all the 128 OTDM tributaries of the 1.28-Tbit/s converted signal.

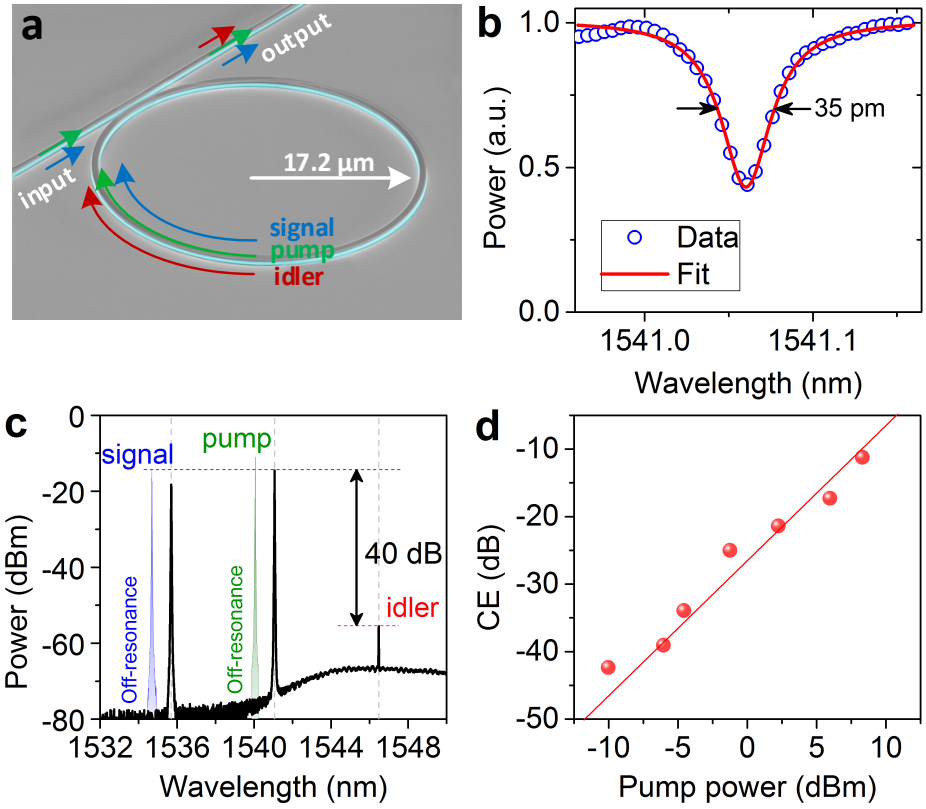

Figure 5 FWM characterization of the AlGaAsOI microresonator

(a) SEM picture of a fabricated AlGaAsOI microresonator with a radius of 17.2 μm.

(b) Measured normalized transmission spectrum of an over-coupled AlGaAsOI microresonator at 1540 nm. The resonance linewidth is ~35 pm which corresponds to a Q factor of 44,000.

(c) Measured output spectra of the microresonator with the pump and signal waves off-resonance (colored curves) and on-resonance (black curve). The light gray dashed lines show the resonance wavelengths of the microresonator.

(d) Measured FWM conversion efficiency (CE) for the microresonator as a function of the pump power in the bus waveguide.

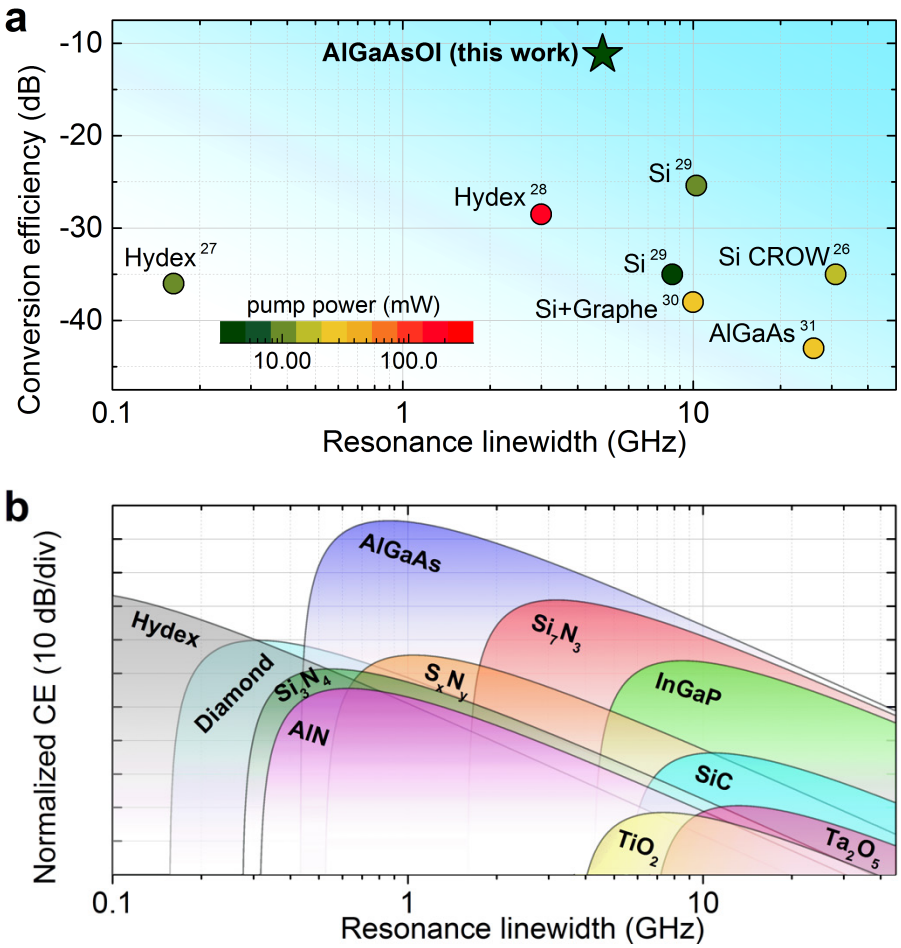

Figure 6 CW-FWM performance comparison for microresonators

(a) Summary of experimentally achieved conversion efficiency versus the resonance linewidth for microresonators in different material platforms.

(b) Estimated FWM performance for microresonators in emerging two-photon absorption (TPA)-free material platforms. The FSRs are assumed the same in the theoretical analysis.

Tables

Table 1. Comparison of strip waveguides in emerging TPA-free nonlinear material platforms

Material platform	n	n_2 (m^2W^{-1})	Dimension (μm^2)	γ ($m^{-1}W^{-1}$)	α (dB cm^{-1})	FOM(γ/ α) (W^{-1})	Reference
Hydex	1.7	1.2×10^{-19}	1.45×1.50	0.22	0.06	0.16	[9]
Si_3N_4	2.0	2.5×10^{-19}	0.71×1.65	1	0.5	0.09	[10]
AlN	2.1	2.3×10^{-19}	0.65×3.50	0.7*	0.6	0.05	[11]
Ta_2O_5	2.1	1.0×10^{-18}	0.40×0.70	5.2	12.6	0.02	[12]
Diamond	2.4	8.2×10^{-20}	0.95×0.85	0.6*	0.34	0.08	[13]
TiO_2	2.4	1.6×10^{-19}	0.25×0.90	1.5	8	0.01	[14]
SiC	2.6	8.0×10^{-18}	0.74×1.40	27*	12.8	0.09	[15]
InGaP	3.1	6.0×10^{-18}	0.25×0.63	475	12	1.7	[16]
S_xN_y	2.1	1.6×10^{-18}	0.30×1.00	16	1.5	0.46	[17]
Si_7N_3	3.1	2.8×10^{-17}	0.30×0.55	500	4.5	4.8	[18]
AlGaAs	3.3	2.6×10^{-17}	0.28×0.64	630	1.3	21	This work

*Derived value according to the available data provided in relevant reference.